

# Probing the structural dynamics of the SNARE recycling machine based on coarse-grained modeling

Wenjun Zheng\*

Department of Physics, State University of New York, Buffalo, New York, 14260

## ABSTRACT

Membrane fusion in eukaryotes is driven by the formation of a four-helix bundle by three SNARE proteins. To recycle the SNARE proteins, they must be disassembled by the ATPase NSF and four SNAP proteins which together form a 20S supercomplex. Recently, the first high-resolution structures of the NSF (in both ATP and ADP state) and 20S (in four distinct states termed I, II, IIIa, and IIIb) were solved by cryo-electron microscopy (cryo-EM), which have paved the way for structure-driven studies of the SNARE recycling mechanism. To probe the structural dynamics of SNARE disassembly at amino-acid level of details, a systematic coarse-grained modeling based on an elastic network model and related analyses were performed. Our normal mode analysis of NSF, SNARE, and 20S predicted key modes of collective motions that partially account for the observed structural changes, and illuminated how the SNARE complex can be effectively destabilized by untwisting and bending motions of the SNARE complex driven by the amino-terminal domains of NSF in state II. Our flexibility analysis identified regions with high/low flexibility that coincide with key functional sites (such as the NSF-SNAPs-SNARE binding sites). A subset of hotspot residues that control the above collective motions, which will make promising targets for future mutagenesis studies were also identified. Finally, the conformational changes in 20S as induced by the transition of NSF from ATP to ADP state were modeled, and a concerted untwisting motion of SNARE/SNAPs and a sideways flip of two amino-terminal domains were observed. In sum, the findings have offered new structural and dynamic details relevant to the SNARE disassembly mechanism, and will guide future functional studies of the SNARE recycling machinery.

Proteins 2016; 84:1055–1066.  
© 2016 Wiley Periodicals, Inc.

**Key words:** 20S supercomplex; coarse-grained modeling; disassembly; elastic network model; flexibility; hotspot; normal mode analysis; NSF; SNAP; SNARE.

## INTRODUCTION

In eukaryotic cells, membrane fusion is driven by zippering of a complex of SNARE (soluble N-ethylmaleimide sensitive factor attachment protein receptors) proteins into a highly stable four-helix bundle.<sup>1,2</sup> To recycle SNARE proteins for multiple rounds of membrane fusion, the ATPase NSF (N-ethylmaleimide sensitive factor) and SNAPs (soluble NSF attachment protein) are recruited to disassemble the SNARE complex into three protein components,<sup>3–5</sup> which is powered by the energy from ATP hydrolysis in only one round of ATP turnover.<sup>6</sup> In mammals, a single NSF gene, together with three different SNAP homologs,<sup>7,8</sup> are responsible for disassembling dozens of different SNARE complexes,<sup>9</sup> hinting for the involvement of non-specific interactions (e.g., electrostatic forces<sup>10</sup>). NSF, first found in

1988,<sup>11,12</sup> is a member of the AAA+ (ATPases associated with diverse cellular activities) superfamily of ATPases<sup>13</sup> forming a homomeric hexamer with a double-ring shape, and each chain is comprised of an amino-terminal domain (named N) and two ATPase domains (named D1 and D2) [see Fig. 1(a)]. The D1 and D2 domains are primarily responsible for the ATPase activity and hexamerization,<sup>14</sup> respectively. The N domains are involved in binding with SNAPs and

Additional Supporting Information may be found in the online version of this article.

Grant sponsor: American Heart Association; Grant number: #14GRNT18980033;

Grant sponsor: National Science Foundation; Grant number: #0952736.

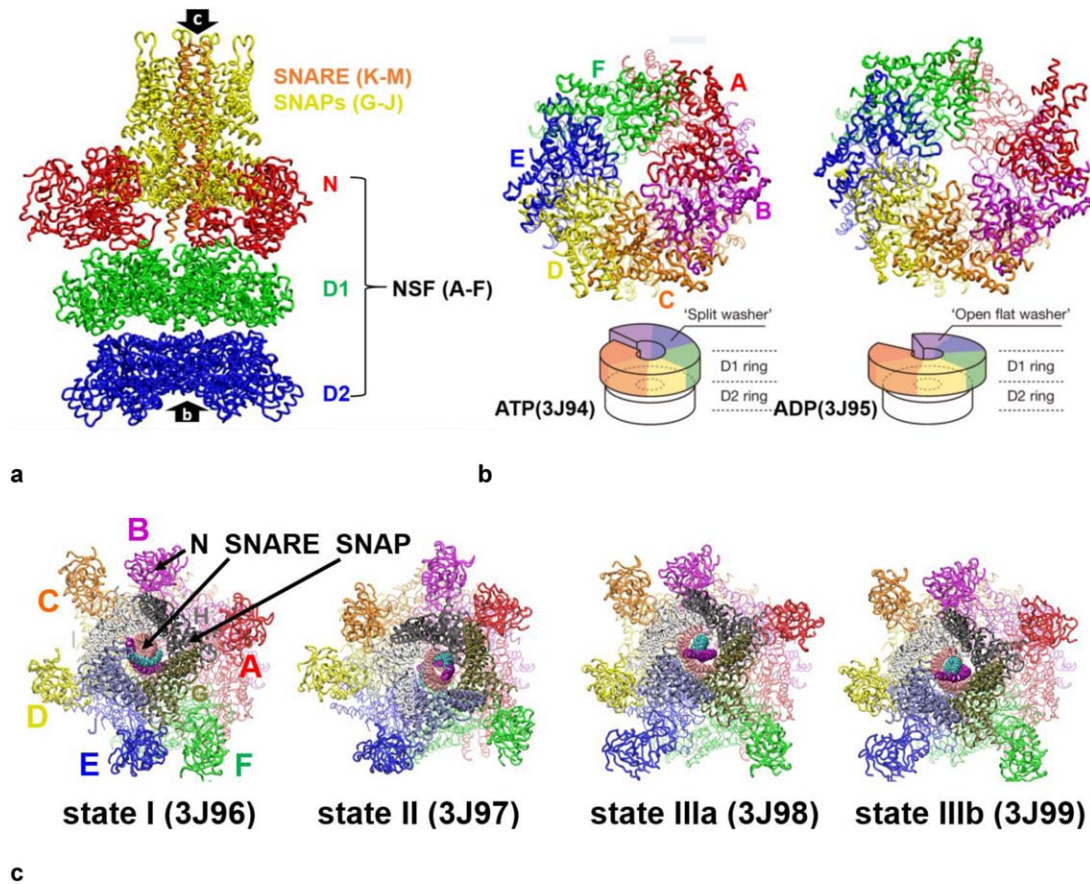
\*Correspondence to: Wenjun Zheng; 239 Fronczak Hall, Buffalo, NY 14260.

E-mail: wjzheng@buffalo.edu

Received 3 February 2016; Revised 4 April 2016; Accepted 13 April 2016

Published online 18 April 2016 in Wiley Online Library (wileyonlinelibrary.com).

DOI: 10.1002/prot.25052

**Figure 1**

Structural architecture of the 20S supercomplex and NSF hexamer. (a) Sideview of 20S (PDB id: 3J97) where the N, D1, and D2 domains of NSF (chain A–F), the SNAPs (chain G–J), and SNARE complex (chain K–M) are colored *red*, *green*, *blue*, *yellow*, and *orange*, respectively; the viewing directions of (b) and (c) are shown by two black arrows labeled with b and c. (b) Bottom view of ATP-bound and ADP-bound NSF where the D1 and D2 domains of NSF are shown as opaque and transparent tubes, respectively; the six NSF chains are colored differently: A (*red*), B (*magenta*), C (*orange*), D (*yellow*), E (*blue*), F (*green*); the ATP-bound and ADP-bound NSF structure resemble a split washer and an open flat washer, respectively (see Ref. 10). (c) Top view of 20S in four states (termed I, II, IIIa, and IIIb) where the N domains of NSF, SNAPs, and SNARE are shown as opaque tubes, and colored by chain [NSF: same color scheme as (b); SNAPs: G (*tan*), H (*gray*), I (*white*), J (*iceblue*); SNARE: K (*cyan*), L (*purple*), M (*pink*)]; the rest of NSF is transparent. In SNARE, chain K, L, and M correspond to VAMP2, Syntaxin-1A, and SNAP-25, respectively.

SNARE.<sup>15</sup> Together, the NSF, SNAPs, and SNARE complex form the so-called 20S supercomplex acting as a SNARE recycling machine.<sup>3</sup>

At atomic resolutions, the crystal structures of the D2 and the N domains of NSF were previously determined.<sup>16–19</sup> At lower resolutions ( $>11\text{\AA}$ ), electron microscopy (EM) techniques were used to visualize the full-length NSF and the 20S supercomplex,<sup>4,20–23</sup> which offered a glimpse to their global architecture. However, due to limited resolutions, these EM studies could not clearly resolve densities for D1 domains, SNAPs, and SNARE complex, leaving the detailed molecular mechanism of SNARE disassembly largely unknown. In a recent landmark article,<sup>10</sup> the labs of Cheng and Brunger used single-particle cryo-EM to solve the first high-resolution structures of full-length NSF in two different nucleotide states [ATP and ADP-bound state, at 4.2 and 7.6 Å

resolution, respectively, see Fig. 1(b)], and four distinct structures of 20S [termed states I, II, IIIa, and IIIb, see Fig. 1(c)] with resolutions ranging from 7.6 to 8.4 Å. These new structures are complemented by another recent cryo-EM study of the 20S particles at a lower resolution.<sup>24</sup> The 20S supercomplex features a tower architecture with different domains organized into layers [D1 and D2 domains of NSF at the base, and a SNARE complex at the top surrounded by four SNAPs and six N domains of NSF,<sup>10</sup> see Fig. 1(a)]. The cryo-EM structures revealed pronounced asymmetry in NSF and large conformational changes in NSF and 20S [upon ATP hydrolysis and between different 20S states, see Fig. 1(b,c)].<sup>10</sup> Key electrostatic interactions were identified at the interfaces between SNAPs, SNARE, and NSF as confirmed by site-directed mutagenesis.<sup>10</sup> These conformational changes and interactions were proposed to couple

ATP hydrolysis to the production of forces/torques that mechanically disassemble the SNARE complex via unwinding and loosening of the SNARE complex.<sup>10</sup> In particular, the observation of opposite twist for the right-handed SNAREs and the left-handed SNARE helical bundle supports the key role of an untwisting rotation in destabilizing the SNARE complex.<sup>10</sup> The new structures have paved the way for structure-driven investigations of the molecular mechanism of NSF-mediated SNARE complex disassembly. Nevertheless, the dynamic details of SNARE disassembly cannot be directly obtained from these static views of 20S offered by cryo-EM.

Molecular dynamics (MD) simulation is the method of choice for exploring protein dynamics under physiological conditions with atomic resolution.<sup>25</sup> MD has been widely used to study increasingly larger protein complexes. In particular, MD simulation was previously employed to study the SNARE complex<sup>26–30</sup> and membrane fusion.<sup>31,32</sup> In Refs. 26 and 29, the steered MD simulation was used to probe the mechanical unfolding pathway of the SNARE complex. In Ref. 27, the mechanical coupling via the SNARE protein syntaxin 1A was studied by MD with focus on the mechanical properties of a juxtamembrane linker. In Ref. 28, a molecular dynamics simulation of the SNARE complex was carried out in the oxidized and reduced states to explain how oxidation leads to a dysfunctional SNARE complex. However, MD simulation is computationally expensive, especially for large protein complexes in explicit solvent. Typical speed of MD simulation on a single computer node equipped with graphics processing unit is 1–10 nanoseconds per day for a system of up to  $10^5$  atoms, although much higher speed can be achieved on a massively parallelized or special-purpose supercomputer.<sup>33</sup> It remains difficult for MD simulation to access microseconds—seconds time scales relevant to many functionally important conformational transitions of protein complexes. As shown by both ensemble and single-molecule methods (see a review<sup>34</sup>), the reaction of SNARE disassembly by NSF spans tens of seconds, which is far beyond the reach of MD simulation. Additionally, the 20S supercomplex poses a tremendous challenge to MD simulation because of its enormous size (with >5400 amino acids).

To overcome the time-scale limit of MD simulation, coarse-grained modeling has been vigorously pursued using reduced protein representations (e.g., one bead per amino acid residue) and simplified force fields (e.g., harmonic potential).<sup>35,36</sup> As a popular coarse-grained model, the elastic network model (ENM) is constructed by connecting nearby  $C_\alpha$  atoms with harmonic springs.<sup>37–39</sup> Despite its simplicity, the normal mode analysis (NMA) of ENM can be used to predict a few low-frequency modes of collective motions, which often compare well with conformational changes observed between experimentally solved protein struc-

tures in different functional states.<sup>40</sup> Numerous studies have established ENM as a useful and efficient means to probe structural dynamics of large protein complexes (including those structurally similar to the 20S supercomplex, such as another AAA+ protein dynein,<sup>41</sup> the hexameric  $F_1$  ATPase,<sup>42</sup> and a double-ring chaperonin GroEL<sup>43</sup>) with virtually no limit in timescale or system size (see reviews<sup>44,45</sup>). Unlike MD simulation, ENM-based coarse-grained modeling does not require complete all-atom protein structures and is more robust to imperfection in initial structures (such as missing residues and lower resolution in some structural parts); therefore, it is highly suitable for application to the newly solved cryo-EM structures of 20S supercomplex.<sup>10</sup>

In this study, we will employ ENM and related modeling/analysis tools to yield detailed insights to the functional motions of NSF, SNARE, and 20S relevant to the SNARE disassembly process.

## MATERIALS AND METHODS

### Elastic network model and related flexibility and hotspot analysis

In an ENM, a protein structure is represented as a network of  $C_\alpha$  atoms of amino acid residues. Harmonic springs link all pairs of  $C_\alpha$  atoms within a cutoff distance  $R_c$  chosen to be 25 Å. A large  $R_c$  ensures good local connectivity of the ENM.

The ENM potential energy is:

$$E = \frac{1}{2} \sum_{i=1}^N \sum_{j=1}^{i-1} k_{ij} \theta(R_c - d_{ij,0}) (d_{ij} - d_{ij,0})^2, \quad (1)$$

where  $N$  is the number of  $C_\alpha$  atoms,  $\theta(x)$  is the Heaviside function,  $d_{ij}$  is the distance between the  $C_\alpha$  atom  $i$  and  $j$ ,  $d_{ij,0}$  is the value of  $d_{ij}$  as given by a protein structure (e.g., a structure of SNARE, NSF, or 20S supercomplex). The spring constant  $k_{ij}$  is set to be  $(4/d_{ij,0})^6$  for non-bonded interactions (following Refs. 46 and 47) and 10 for bonded interactions (in arbitrary unit). We have also tried other ENM schemes [e.g., distance-independent spring constant with  $R_c = 10$  Å, or other distance-dependence like  $(4/d_{ij,0})^2$ ], and verified that the NMA results are not sensitive to the choice of ENM schemes.

The NMA solves the following eigen equation for a Hessian matrix  $H$  which is obtained by calculating the second derivatives of ENM potential energy (see Ref. 48):

$$HV_m = \lambda_m V_m, \quad (2)$$

where  $\lambda_m$  and  $V_m$  represent the eigenvalue and eigenvector of mode  $m$ , respectively. After excluding six zero modes corresponding to three rotations and three

translations, we number non-zero modes starting from 1 in the order of ascending eigenvalue.

To assess the relevance of each mode (calculated for the SNARE complex) to SNARE disassembly, we calculate the following two forms of partial distortion energy related to SNARE disassembly:

$E_1$ : A summation of elastic interactions [see Eq. (1)] for residue pairs (i, j) with either i or j from the C-terminal part of VAMP2 (residues 56–89) which unzips from the rest of SNARE to form a “half-zipped” intermediate state during mechanical unfolding.<sup>49,50</sup>

$E_2$ : A summation of elastic interactions for inter-chain residue pairs (i, j) which are relevant to the dissociation of three SNARE proteins.

The above two forms of partial distortion energy are then divided by the total energy  $E = \lambda_m$  for mode m to allow comparison between different modes.

For mode m, a perturbation analysis is used to assess how much the eigenvalue changes (represented as  $\delta\lambda_m$ ) in response to a perturbation at a chosen residue position<sup>51–53</sup> (i.e., by uniformly weakening the springs connected to this position to mimic an Alanine mutation). Then we average  $\delta\lambda_m/\lambda_m$  over the lowest 20 modes to assess the overall dynamic importance of this residue position:

$$\langle \delta\lambda/\lambda \rangle = \frac{1}{20} \sum_{m=1}^{20} \delta\lambda_m/\lambda_m \quad (3)$$

To validate ENM-based NMA, we compare each mode (i.e., mode m) with the observed structural change  $X_{\text{obs}}$  between two superimposed protein structures by calculating the following overlap<sup>41</sup>:

$$I_m = X_{\text{obs}} \cdot V_m / |X_{\text{obs}}| \quad (4)$$

$|I_m|$  varies between 0 and 1 with higher value meaning greater similarity.  $I_m^2$  gives the fractional contribution of mode m to  $X_{\text{obs}}$ . The cumulative squared overlap  $C_M = \sum_{m=1}^M I_m^2$  gives the fractional contribution of the lowest  $M = 20$  modes to  $X_{\text{obs}}$ .<sup>41</sup>

To assess the local flexibility at individual residue positions as described by the lowest  $M = 20$  modes, we define the following cumulative flexibility (CF)<sup>54</sup>:

$$CF_n = \sqrt{\sum_{m=1}^M (|V_{m,nx}|^2 + |V_{m,ny}|^2 + |V_{m,nz}|^2)}, \quad (5)$$

where,  $V_{m,nx}$ ,  $V_{m,ny}$ , and  $V_{m,nz}$  are the x, y, and z component of mode m's eigenvector at residue position n. An alternative eigenvalue-weighted CF was also calculated (see Fig. S2 in Supporting Information).

## Coarse-grained modeling of conformational changes in 20S as induced by ATP hydrolysis in NSF

We previously developed an interpolated ENM (iENM) protocol to construct a transition pathway (that is, a series of intermediate conformations) between two given protein conformations based on a double-well potential built from these two conformations<sup>55</sup> (available at a webserver [http://enm.lobos.nih.gov/start\\_ienm.html](http://enm.lobos.nih.gov/start_ienm.html)). The iENM protocol can be adapted to model an unknown activated conformation from a known inactivated conformation together with a target conformation of the activation domain. The idea is to progressively transform the activation domain toward its target conformation and let the rest of protein relax to a series of minimal-energy conformations leading to a final model for the unknown activated conformation.<sup>41,54</sup> Here we use the iENM to model conformational changes in 20S upon transforming the NSF (as the activation domain) from the ATP-bound conformation (PDB id: 3J94) to the ADP-bound conformation (PDB id: 3J95). Then we project the predicted conformational changes in 20S along the lowest 20 modes (solved by NMA of ENM, see above) to identify the key modes of collective motions activated by ATP hydrolysis in NSF.

## RESULTS AND DISCUSSION

In what follows, we will present results of using ENM-based NMA to analyze key modes of collective motions, flexibility, and hotspot residues in NSF, SNARE, and 20S. Then we will model the conformational changes in 20S as induced by ATP hydrolysis in NSF.

### NMA predicts key collective motions, flexible regions, and hotspot residues in NSF

As revealed by cryo-EM,<sup>10</sup> the NSF hexamer (comprised of chains A–F) undergoes large conformational changes upon ATP hydrolysis [i.e., from “split washer” to “open flat washer,” see Fig. 1(b)]. Additionally, the D1/D2 ring of NSF tightens up upon binding with SNAPs and SNARE.<sup>10</sup> Here we will analyze these observed changes in terms of collective motions as predicted by the ENM-based NMA (see “Methods” section).

Starting from the ATP-bound structure of NSF (PDB id: 3J94), we constructed a  $C_\alpha$ -only ENM by linking each pair of residues within a cutoff distance by a harmonic spring with a distance-dependent force constant (see “Methods” section). Then we used NMA (see “Methods” section) to obtain a spectrum of total 8685 modes, and focused on the lowest 20 modes, each describing a specific pattern of collective motions energetically favored by the given NSF structure (e.g., with minimal cost of elastic energy). Such structurally encoded motions are

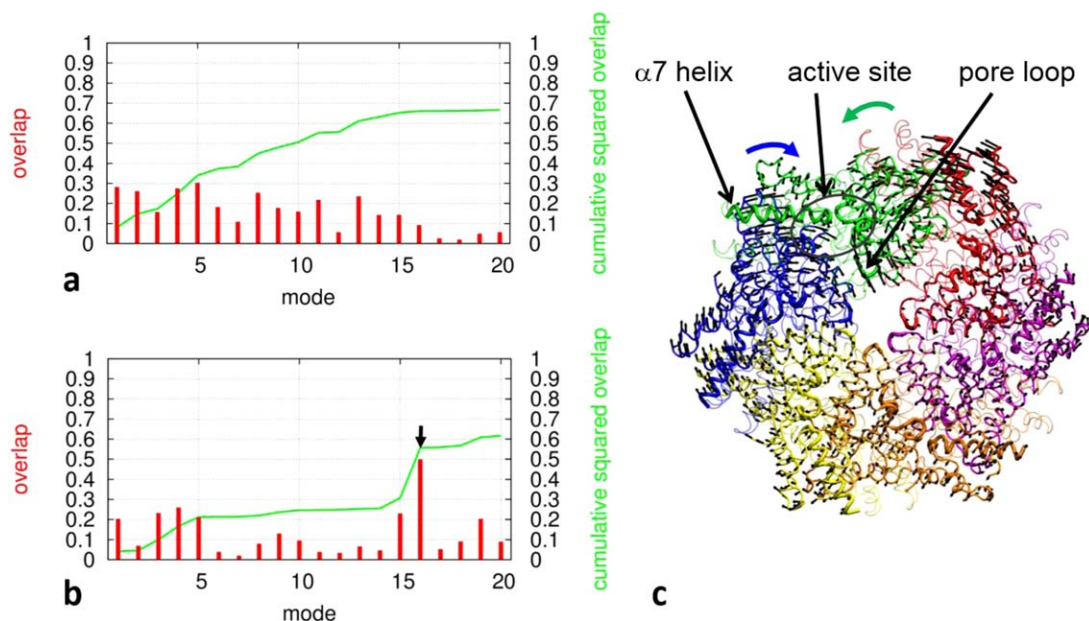


**Figure 2**

Results of NMA for NSF. (a) The overlap (red) and cumulative squared overlap (green) between the 20 lowest modes and the observed structural changes from the ATP-bound NSF (PDB id: 3J94) to the ADP-bound NSF (PDB id: 3J95). (b) The overlap (red) and cumulative squared overlap (green) between the 20 lowest modes and the observed structural changes from the ATP-bound NSF (PDB id: 3J94) to the NSF structure in a 20S supercomplex in state II (PDB id: 3J97). (c) The motional pattern of mode 16 as depicted by a vector plot (with black vectors representing displacements of individual residues in the D1 domains of NSF, and using the same color scheme as Fig 1b).

likely to be functionally important as shown by many previous studies (see reviews<sup>44,45</sup>).

For validation of these lowest modes, we assessed how well they collectively capture the observed conformational changes from the ATP-bound structure to the ADP-bound structure of NSF (PDB id: 3J95). To this end, we calculated the overlap between each mode and the observed conformational changes and the cumulative squared overlap of the lowest 20 modes (see “Methods” section). Encouragingly, approximately 66% of the observed large conformational changes (RMSD = 8.4 Å) are captured by the lowest 20 modes, with as many as seven modes significantly involved (overlap >0.2) but no dominant mode [see Fig. 2(a)]. The involvement of multiple modes is often observed for those protein conformational transitions from a closed form to an open form due to the need for breaking many inter-residue contacts. The collective motions described by these modes can be energetically driven by ATP hydrolysis in NSF.

The above validating calculation was also done for the observed conformational changes in NSF upon substrate binding [that is, from 3J94 to the NSF structures within the four 20S structures<sup>10</sup> (PDB ids: 3J96, 3J97, 3J98, and 3J99)]. Reassuringly, we found the lowest 20 modes capture 55%–62% of the observed conformational changes, where mode 16 dominates with a maximal overlap of 0.46–0.50 [see Fig. 2(b) and Supporting Information

Table S1]. Indeed, mode 16 features pronounced rotations of D1 domains in the E and F chain of NSF, resulting in closing of the E–F interface of D1-ring [see Fig. 2(c)]. These rotations account for the tightening of the NSF rings as observed between isolated NSF and substrate-bound NSF.<sup>10</sup> The dominance of a single mode is common for those protein conformational transitions from a loosely packed form to a tightly packed form.

In sum, greater than 50% of the observed structural changes in NSF upon ATP hydrolysis and substrate binding are captured by the 20 lowest modes (i.e., only 0.2% of all modes), although the former is dynamically more complex (e.g., involving more modes) than the latter. These findings give strong support to the use of ENM-based NMA to analyze functional motions in NSF.

To analyze the flexibility of NSF using the lowest 20 modes, we calculated the cumulative flexibility (denoted CF, see “Methods” section) at individual residue positions of ATP-bound and ADP-bound NSF (see Fig. 3). Chain F is the most flexible in the ATP-bound NSF [see Fig. 3(a)]. The ADP-bound NSF differs from the ATP-bound NSF with higher flexibility in the C and N terminal region of D1 domains of chain A and F, respectively [see Fig. 3(c)]. This is consistent with the lower resolution of the ADP-bound NSF structure.<sup>10</sup> We focused the flexibility analysis on the following key motifs in the D1 domains of NSF [see Fig. 3(c)]:

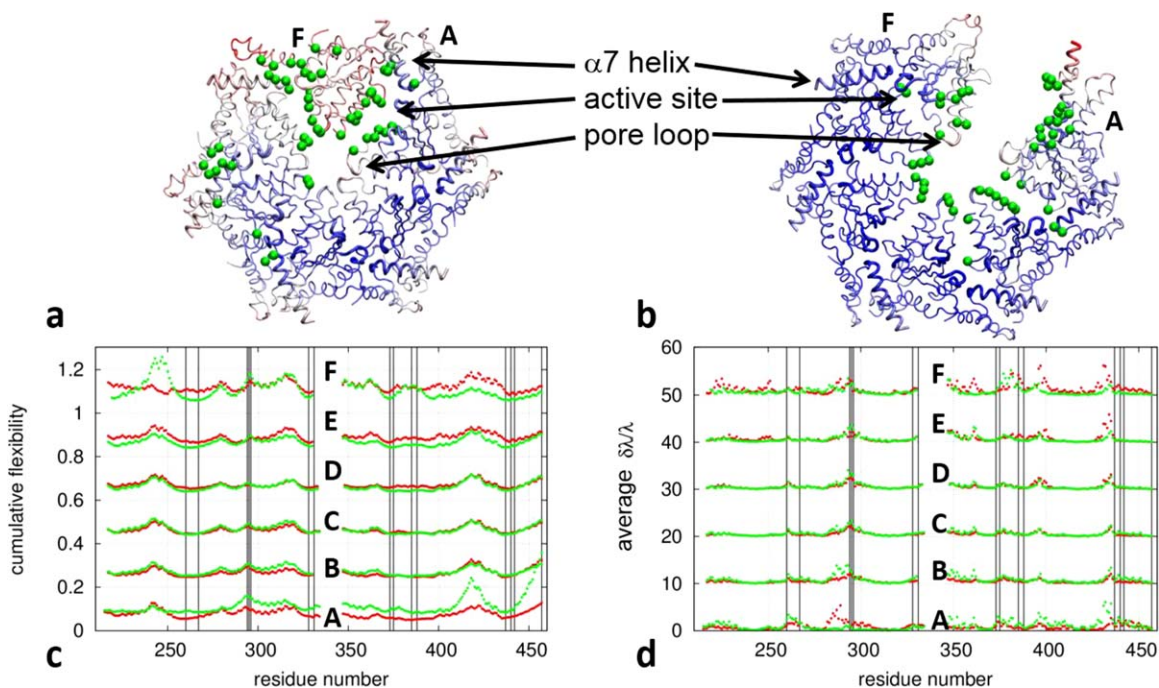


**Figure 3**

Results of flexibility and hotspot analysis for NSF. (a) Bottom view of the D1 ring of ATP-bound NSF (PDB id: 3J94). (b) Bottom view of the D1 ring of ADP-bound NSF (PDB id: 3J95). (c) CF as a function of residue position for the D1 domains of chain A-F in NSF. (d) Average  $\delta\lambda/\lambda$  as a function of residue position for the D1 domains of chain A-F in NSF. In (a) and (b), active-site residues (260–267, 328–331, 373–375, 385, 388, and 440–442), pore loops (294–296), and  $\alpha 7$  helices (437–457) are represented by thick tubes. The above key residues are also marked by vertical lines in (c) and (d). In (a) and (b), the structure is colored by CF (with blue and red corresponding to low and high CF, respectively), and the green balls represent hotspot residues in the D1 domains. In (c) and (d), the data points of ATP-bound and ADP-bound NSF are colored red and green, respectively.

- At the active sites of ATP hydrolysis, most residues have low flexibility [corresponding to valleys in the CF plot, see Fig. 3(c)], except in chain A and F of the ADP-bound NSF where those active-site residues exposed to the A-F gap are highly flexible [corresponding to peaks in the CF plot at residues R385 and R388 in chain F, see Fig. 3(c)].
- The pore loops (residues Y294, V295, and G296) correspond to peaks in the CF plot, which are more pronounced in the ADP-bound state [particularly in chain A and E, see Fig. 3(c)].
- The  $\alpha 7$  helices (residues 437–457) exhibit high flexibility toward the C-terminus, which is especially pronounced in chain A of the ADP-bound NSF [see Fig. 3(c)].

In sum, our finding of highly flexible pore loops and  $\alpha 7$  helices is consistent with the proposal that these key parts dynamically couple the ATPase active sites to global conformational changes in the NSF and 20S supercomplex.<sup>10</sup>

Next, we used an ENM-based perturbation analysis (see “Methods” section) to identify a subset of hotspot residues that control the collective motions described by the lowest 20 modes (see Fig. 3 and Supporting Informa-

tion Table S2). To this end, we calculated for each residue position a score  $\langle\delta\lambda/\lambda\rangle$  to assess the overall dynamic importance of this residue position to the lowest 20 modes [see “Methods” section and Fig. 3(d)]. We selected top 3% hotspot residue positions as ranked by  $\langle\delta\lambda/\lambda\rangle$ . In the ATP-bound NSF, the hotspot residues are clustered at the interfaces between chain F and two adjacent chains [chain A and E, see Fig. 3(a)], overlapping with the active sites (e.g., R385 of chain F), pore loops (e.g., Y294 and V295 of chain D and F) and the N-terminal hinge regions of  $\alpha 7$  helices (e.g., residues 431–435). In the ADP-bound NSF, the hotspot residues are distributed along the A–F gap and central pore regions [including the pore loops of chains B, C, D, and E, see Fig. 3(b)].

In sum, the predicted hotspot residues overlap well with key functional motifs of NSF, including the ATPase active sites, the pore loops, and the  $\alpha 7$  helices. Given the involvement of these key residues in functional motions and couplings as shown in previous studies,<sup>51–53,56</sup> we predict that these hotspot residues dynamically couple the ATPase activity of NSF to downstream conformational changes propagating between adjacent NSF subunits (via  $\alpha 7$  helices) and toward SNARE (via pore

loops).<sup>10</sup> Because the ENM does not incorporate the biochemical properties of amino acids, the hotspot positions are predicted solely based on the mechanical and dynamical properties of the model. As shown by previous studies, the ENM-predicted mechanically/dynamically important sites are evolutionally conserved,<sup>51,53</sup> and co-localized with key biochemical sites (e.g., active sites of enzymes<sup>57</sup>) or disease-mutation sites.<sup>58</sup> These findings strongly support the functional relevance of the ENM-predicted sites and the functional importance of biomolecular mechanics and dynamics as captured by the ENM.

### NMA of the SNARE complex reveals collective motions that drive SNARE disassembly

The truncated neuronal SNARE complex is a four-helix bundle composed of three proteins: syntaxin-1A, synaptobrevin-2/VAMP-2 (vesicle-associated membrane protein 2), and SNAP-25 (synaptosomal-associated protein 25). As revealed by a recent single-molecule study, the SNARE complex unzippers through three sequential steps via a half-zipped intermediate with the C-terminal section of VAMP-2 unzipped from the rest of SNARE, followed by dissociation of the three proteins.<sup>50</sup> Here we will employ ENM-based NMA to study how the SNARE disassembly process is facilitated by the collective motions in the SNARE complex induced by binding with SNAPs and NSF in the 20S supercomplex.

In the 20S structures (PDB ids: 3J96, 3J97, 3J98, and 3J99, corresponding to state I, II, IIIa, and IIIb), the SNARE complex was modeled by fitting the cryo-EM densities starting from a crystal structure of truncated SNARE complex (PDB id: 1N7S, with 1.45 Å resolution), resulting in small but significant conformational changes (RMSD  $\leq 1.9$  Å) due to binding of SNARE with SNAPs and NSF.<sup>10</sup> To assess the relevance of these states to the SNARE disassembly, we will analyze these observed conformational changes in terms of collective motions as predicted by ENM-based NMA (see “Methods” section). To this end, we built an ENM based on the  $C_{\alpha}$  coordinates of 1N7S and performed NMA for the ENM (see “Methods” section). Then we calculated the overlap between each mode and the observed conformational change from 1N7S to each 20S structure and the cumulative squared overlap of the lowest 20 modes (see “Methods” section and Supporting Information Table S3):

a. The 1N7S-to-3J96 conformational change in SNARE is the smallest among them (with RMSD = 1.1 Å), with mode 3 contributing the most (overlap = 0.36). The lowest 20 modes account for 48% of this observed change, which is higher than the cumulative squared overlap for the other 20S structures (see Supporting Information Table S3). These findings sug-

gest that the SNARE complex is least distorted in state I compared with the other 20S structures.

- b. The 1N7S-to-3J97 conformational change in SNARE is the largest among them (with RMSD = 1.9 Å), with mode 2 contributing the most (overlap = 0.26) followed by mode 3 (overlap = 0.23). Only 32% of this observed change is accounted for by the lowest 20 modes, which is lower than the cumulative squared overlap for the other 20S structures (see Supporting Information Table S3). Therefore, the SNARE complex is most distorted in state II compared with the other 20S structures.
- c. The 1N7S-to-3J98/3J99 conformational change is intermediate in RMSD (with RMSD = 1.6 Å), with mode 3 contributing the most (overlap = 0.27). The lowest 20 modes account for 38% of this observed change. Therefore, the distortion of SNARE complex in state IIIa and IIIb is intermediate between state I and II.

Taken together, the above results suggest the following order for the four 20S states in terms of their ability to structurally distort the SNARE complex: state I (3J96) < state IIIa and IIIb (3J98 and 3J99) < state II (3J97).

Next, we visualized the lowest three modes which capture three distinct collective motions that are energetically favorable to the SNARE four-helix bundle. Mode 1 and 2 describe two orthogonal bending motions of SNARE hinged at the middle [see Supporting Information Fig. S1(a,b)]. Mode 3 describes a twisting motion around the long axis of the four-helix bundle [see Supporting Information Fig. S1(c)]. Compared with mode 1 and 2, mode 3 incurs greater distortion energy involving the C-terminal region of VAMP2 and inter-chain contacts (assessed by  $E_1/E$  and  $E_2/E$ , see “Methods” section and Supporting Information Table S3). Therefore, mode 3 contributes most to the SNARE disassembly among the three modes. Further supporting its importance, mode 3 is also more involved in the observed conformational changes in SNARE than mode 1 and 2 (with overlap > 0.2, see Supporting Information Table S3), and is strongly coupled with the key mode solved from the 20S structure in state II (see below). Going from 1N7S to those 20S structures, mode 3 causes the left-hand-twisted four-helix bundle to untwist [Supporting Information Fig. S1(c)], which is expected to loosen the four-helix bundle and cause the SNARE proteins to disassociate. All three modes of motions are hinged in the middle (near the ionic layer), which is in proximity to a patch of basic residues in SNAPs (including K122 and K163).<sup>10</sup> By modulating the above three modes, the ionic layer may enable force transmission from SNAPs to the SNARE complex to drive the collective motions (e.g., untwisting) for SNARE disassembly.

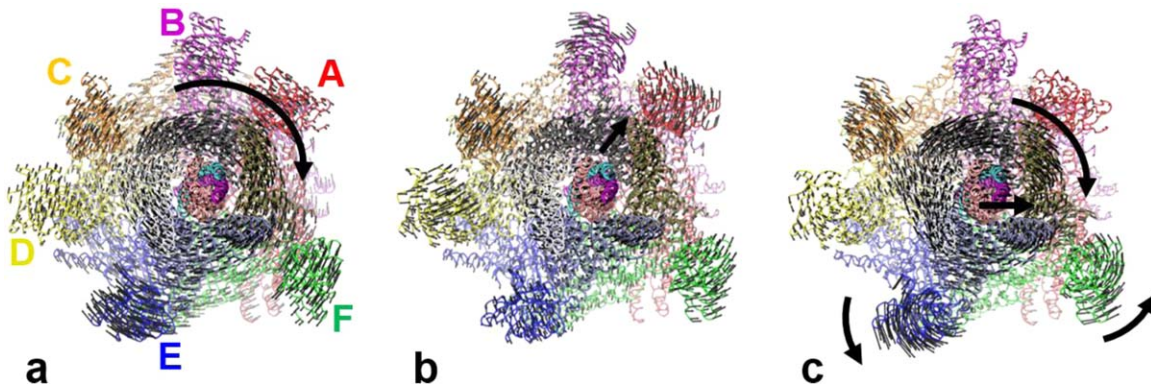


**Figure 4**

Results of NMA for state II of 20S (PDB id: 3J97). The motional pattern of (a) mode 1, (b) mode 7, and (c) mode 9 as depicted by a vector plot (with *black vectors* representing displacements of individual residues, and using the same color scheme and top view as Fig 1c). The bold arrows show directions of rotation and shift of the N domains of NSF, SNAPs, and SNARE complex.

In sum, our NMA of the SNARE complex has pinpointed the 20S state II as the most relevant to the SNARE disassembly, which likely involves untwisting and bending motions of the SNARE complex that destabilize the SNARE four-helix bundle. While our focus is on the global twisting/bending motions in SNARE, it is possible that other modes of motions may also contribute to the SNARE disassembly dynamics.

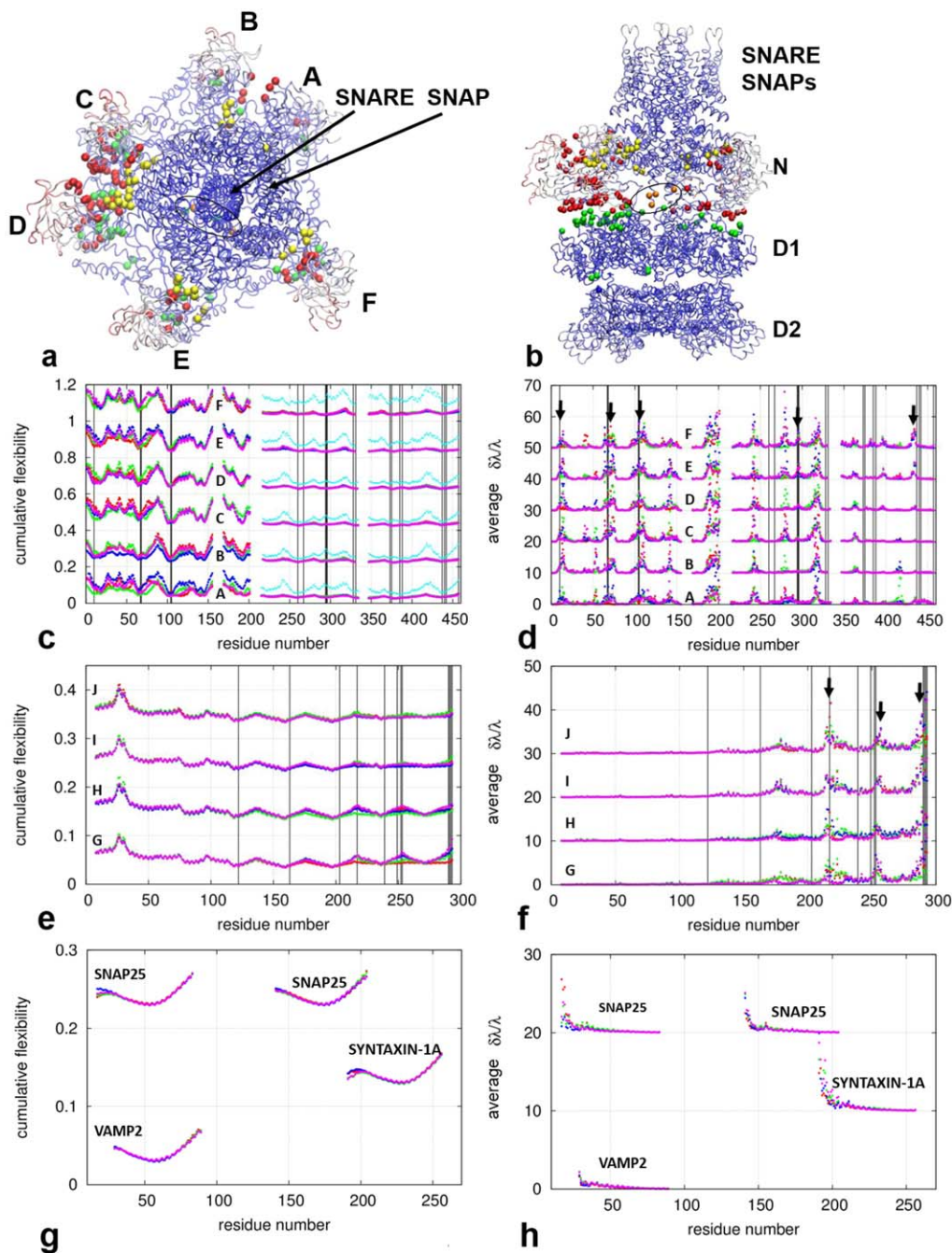
#### **NMA of the 20S structures predicts key collective motions, high/low-flexibility regions, and hotspot residues**

The cryo-EM study<sup>10</sup> identified four distinct structures/states of the 20S supercomplex (denoted I, II, IIIa, and IIIb, for 3J96, 3J97, 3J98, and 3J99, respectively), featuring different modes of coordination between six N domains of NSF (chain A–F) and four SNAP molecules [chain G–J, see Fig. 1(c)]. It was speculated that conformational changes in or between these states may facilitate disassembly of the SNARE complex.<sup>10</sup> To substantiate this hypothesis, we performed ENM-based NMA for these 20S structures and analyzed the lowest 20 modes in comparison with the observed changes between them (see Supporting Information Table S1).

Starting from 3J96 (state I), only 39%–48% of the observed conformational changes to the other 20S states were captured by the lowest 20 modes, which is lower than the cumulative squared overlap for the other 20S structures (see Supporting Information Table S1). This is consistent with the observation that 3J96 features close packing between chain E and F [both coordinating with the same SNAP molecule, see Fig. 1(c)], while in the other three 20S structures chain E and F are separated [each coordinating with a different SNAP molecule, see Fig. 1(c)]. Therefore, the transitions from 3J96 to the

other states are energetically unfavorable due to the need for breaking numerous E–F contacts. The E–F contacts may restrain the motions of chain E and F, thus reduce their ability to mechanically disassemble the SNARE complex directly (via the pore loops) or indirectly (via SNAPs). This explains the finding that the SNARE complex is less distorted in 3J96 than in the other 20S structures (see above). Therefore, we propose that state I captures an inactive or partially active 20S state where NSF and SNAPs cannot effectively disassemble the SNARE complex.

Starting from 3J97 (state II), as high as 55%–68% of the observed conformational changes to the other 20S states were captured by the lowest 20 modes (see Supporting Information Table S1), with two top-contributing modes (mode 1 and 9, see Fig. 4). Toward the direction of state IIIa and IIIb, mode 1 involves a concerted clockwise rotation of all six N domains of NSF together with SNAPs and SNARE relative to the D1/D2 ring of NSF [in the top view, see Fig. 4(a)], which causes the left-hand-twisted SNARE complex to twist further [via the twisting mode 3 of SNARE, see Supporting Information Fig. S1(c)], therefore become more tightly packed and more stable. Mode 9 shows a clockwise twisting of SNAPs, a sideway bending of the SNARE complex, accompanied by counterclockwise swiveling of the N domains in chain E and F [in the top view, see Fig. 4(c)]. In contrast to the other 20S structures, 3J97 features minimal inter-subunit contacts involving the N domains of chain E and F [see Fig. 1(c)], enabling them to undergo large motions. Additionally, the SNARE complex is more distorted in 3J97 than in the other 20S structures (see above). Taking the above evidence together, we propose that state II captures an active 20S state where NSF and SNAPs can effectively disassemble the SNARE complex by triggering mode 1 and 9, which

**Figure 5**

Results of flexibility and hotspot analysis for 20S. (a) Top view of the 20S structure (PDB id: 3J97). (b) Side view of the 20S structure (PDB id: 3J97). (c) CF for the N and D1 domains of NSF (chain A–F). (d) Average  $\delta\lambda/\lambda$  for the N and D1 domains of NSF (chain A–F). (e) CF for the four SNAP molecules (chain G–J). (f) Average  $\delta\lambda/\lambda$  for the four SNAP molecules (chain G–J). (g) CF for the three SNARE proteins (lower curve for VAMP2, middle curve for syntaxin-1A, and upper two curves for SNAP-25). (h) Average  $\delta\lambda/\lambda$  for the three SNARE proteins (lower curve for VAMP2, middle curve for syntaxin-1A, and upper two curves for SNAP-25). In (a) and (b), the 20S structure is colored by CF (with blue and red corresponding to low and high CF, respectively), and the colored balls represent hotspot residues in D2 (blue), D1 (green), N (red) domains of NSF, SNAPs (yellow), and SNARE (orange). In (c) and (d), SNAP-binding residues (10, 67–68, and 104–105), active-site residues (260–267, 328–331, 373–375, 385, 388, and 440–442), pore loops (294–296), and  $\alpha 7$  helices (437–457) are marked by vertical lines. In (e) and (f), NSF-binding residues (217, 249, 252–253, and 290–293) and SNARE-binding residues (122, 163, 203, and 239) are marked by vertical lines. In (c)–(h), the data points for 3J94, 3J96, 3J97, 3J98, and 3J99 are colored cyan, red, green, blue, and purple, respectively. In (d) and (f), the major peaks discussed in the text are pointed to by bold arrows. The data points for different NSF/SNAP subunits and SNARE proteins are shifted vertically for clarity.

mechanically untwist and bend the SNARE complex using the flexible N domains of chain E and F.

Starting from 3J98 (state IIIa) or 3J99 (state IIIb), 48%–71% or 49%–65% of the observed conformational changes to the other 20S states were captured by the lowest 20 modes (see Supporting Information Table S1). Compared with 3J97, 3J98 and 3J99 feature additional close packing between chain D and E, and between chain B and C [see Fig. 1(c)], which may hinder the motions of N domains in these chains. In addition, the SNARE complex is more distorted in 3J97 than in 3J98 or 3J99 (see above). Therefore, we propose that state IIIa and IIIb are less effective than 3J97 in the SNARE disassembly.

In sum, the NMA of 20S structures has identified key modes of untwisting and bending motions driven by the flexible N domains, which may effectively destabilize the SNARE complex in state II.

To analyze the flexibility of 20S using the lowest 20 modes, we calculated the CF at individual residue positions (see Fig. 5). The flexibility of D1 and D2 domains is considerably reduced in the 20S supercomplex than in isolated NSF [see Fig. 5(c)], thanks to the stabilization by binding of SNAPs and SNARE. Within NSF, the N domains are much more flexible than the D1 and D2 domains [see Fig. 5(c)]. We focused the flexibility analysis on the N domains of NSF, SNAPs, and SNARE as follows:

- In the N domains of NSF, the CF plot features pronounced peaks and valleys [see Fig. 5(c)]. Three valleys correspond to key SNAP-binding basic residues (R10, R67, K68, K104, and K105) as found in Ref. 10 and a previous mutagenesis study,<sup>59</sup> which are due to the stabilization of SNAPs binding.
- In SNAPs, three CF peaks correspond to key NSF-binding acidic residues (D217, E249, E252, E253, D290, E291, E292, and D293), which are most pronounced in chain G [see Fig. 5(e)]. Interestingly, chain G of SNAPs is coordinated with the N domain of chain F in NSF which is highly dynamic. Four CF valleys coincide with those SNARE-binding basic residues<sup>60</sup> (K122, K163, K203, and R239) [see Fig. 5(e)]. So the SNAPs-NSF binding interface is more dynamic than the SNAPs-SNARE binding interface.
- In the SNARE complex, a broad CF valley is at the center of the four-helix bundle [see Fig. 5(g)], which can be attributed to SNAPs binding near the central ionic layer of SNARE.<sup>10</sup> The CF plot is peaked near the bottom of the SNARE four-helix bundle [see Fig. 5(g)], where the N-terminal residues of SNAP-25 and syntaxin-1A directly interact with the pore loops of chain E and F in NSF [see circled region in Fig. 5(a,b)].

In sum, our flexibility analysis found high flexibility in the N domains of NSF, and both high and low flexibility at the NSF-SNAPs-SNARE binding interfaces, which is

consistent with the idea that these key domains and interfaces are involved in dynamically coupling NSF to SNAPs and SNARE.

Next, we identified a subset of hotspot residues that control the collective motions as described by the lowest 20 modes (see Fig. 5 and Supporting Information Table S2). To this end, we calculated for each residue position a score  $\langle \delta\lambda/\lambda \rangle$  to assess its overall dynamic importance [see Fig. 5(d,f, h)]. We selected those top 3% hotspot residue positions as ranked by  $\langle \delta\lambda/\lambda \rangle$ .

- The  $\langle \delta\lambda/\lambda \rangle$  plot exhibits pronounced peaks in the D1 and N domains of NSF [see Fig. 5(d)]. Three of them are near key SNAPs-binding basic residues (R10, R67, K68, K104, and K105) found in Ref. 10, one is at the N-terminus of  $\alpha 7$  helices (near residue S437 of chain E and F) which undergo large translation upon ATP hydrolysis,<sup>10</sup> and one is on the pore loops (residues V295 and G296 in chain E and F, respectively) which interact with SNARE directly.<sup>10</sup> The remaining peaks correspond to hotspot residues clustered at the interfaces between neighboring D1 domains, N domains of NSF, and SNAPs [see Fig. 5(a,b)].
- The  $\langle \delta\lambda/\lambda \rangle$  plot shows three major peaks in SNAPs [see Fig. 5(f)], which are near key NSF-binding acidic residues of SNAPs (D217, E249, E252, E253, D290, E291, E292, and D293) as found in Ref. 10.
- In the SNARE complex, the  $\langle \delta\lambda/\lambda \rangle$  plot peaks sharply at the N-termini of SNAP-25 and syntaxin-1A [see Fig. 5(h)], which directly interact with the pore loops of chains E and F in NSF [see circled region in Fig. 5(a,b)]. This finding suggests that the pore loops may directly apply mechanical force to the bottom of SNARE complex, or contribute indirectly as an anchoring point for the N domains and SNAPs to disassemble SNARE.<sup>34</sup> Notably, these mechanisms may be different from the single-molecule mechanical unfolding of SNAREs that starts from the unzipping at the C-terminus of VAMP2.<sup>50</sup>

In sum, the predicted hotspot residues point to key functional sites and interactions in the 20S supercomplex, which is consistent with the functional relevance of the collective motions captured by the lowest ENM modes, and providing promising targets for future mutagenesis studies.

### Coarse-grained modeling of the conformational changes in 20S as induced by ATP hydrolysis in NSF

To understand how ATP hydrolysis in NSF drives conformational changes in the 20S supercomplex leading to the SNARE disassembly, we utilized the iENM method (see “Methods” section) to transform the D1 and D2 domains of NSF from the ATP-bound conformation (PDB id: 3J97) to the ADP-bound conformation (PDB

id: 3J95), and then modeled the resulting conformational changes in the rest of 20S including the N domains of NSF, SNAPs, and SNARE (see Movie S1). The predicted conformational changes feature a concerted counterclockwise twisting of the six N domains of NSF, SNAPs, and SNARE relative to the rest of NSF, followed by an outward flip of the N domains in chain A and B. The latter flip was observed in the cryo-EM structure of ADP-bound NSF<sup>10</sup> (although the flipped N domains are not present in 3J95). To further analyze what modes of collective motions are involved in such conformational changes driven by ATP hydrolysis, we calculated the overlaps with each of the lowest 20 modes solved from 3J97. The top-contributing modes are mode 7 (overlap = 0.45) followed by mode 1 (overlap = 0.29). As expected, mode 7 features a concerted shift of N domains, SNAPs, and SNARE toward chain A and B accompanied by distinct rotations of the N domains [in the top view, see Fig. 4(b)]. Mode 1 involves a concerted counterclockwise rotation of all six N domains of NSF together with SNAPs and SNARE relative to the rest of NSF [in the top view, opposite to the direction shown in Fig. 4(a)], which causes the left-hand-twisted SNARE complex to untwist and become more loosely packed. Together, these modes cause the SNARE complex to destabilize via untwisting and bending motions of SNARE.

## CONCLUSION

In summary, we have performed comprehensive coarse-grained modeling based on ENM and related analyses. The NMA of NSF, SNARE, and 20S predicted key modes of collective motions that account for a significant fraction of the observed structural changes, and illuminated how the SNARE complex can be effectively destabilized by concerted untwisting and bending motions of the SNARE complex driven by the N domains of NSF in state II. Our flexibility analysis identified regions with high/low flexibility that coincide with key functional sites (such as the NSF-SNAPs-SNARE binding sites). We also identified a subset of hotspot residues that control the above collective motions, which will make promising targets for future mutagenesis studies. Finally, we modeled the conformational changes in 20S as induced by the transition of NSF from ATP to ADP state, and observed a concerted untwisting motion of SNARE/SNAPs and a sideway flip of two N domains in agreement with the observation by cryo-EM. Taken together, our findings have offered new structural and dynamic insights to the SNARE disassembly mechanism, and will guide future functional studies of the SNARE recycling machinery.

In future studies, it will be interesting to directly simulate the dynamics of 20S supercomplex starting from the

20S structures, which can sample larger conformational space away from the cryo-EM structures not accessible to NMA.

## ACKNOWLEDGMENT

Computational support was provided by the Center for Computational Research at the University at Buffalo.

## REFERENCES

1. Sutton RB, Fasshauer D, Jahn R, Brunger AT. Crystal structure of a SNARE complex involved in synaptic exocytosis at 2.4 Å resolution. *Nature* 1998;395:347–353.
2. Weber T, Zemelman BV, McNew JA, Westermann B, Gmachl M, Parlati F, Sollner TH, Rothman JE. SNAREpins: minimal machinery for membrane fusion. *Cell* 1998;92:759–772.
3. Sollner T, Bennett MK, Whiteheart SW, Scheller RH, Rothman JE. A protein assembly-disassembly pathway in vitro that may correspond to sequential steps of synaptic vesicle docking, activation, and fusion. *Cell* 1993;75:409–418.
4. Hanson PI, Roth R, Morisaki H, Jahn R, Heuser JE. Structure and conformational changes in NSF and its membrane receptor complexes visualized by quick-freeze/deep-etch electron microscopy. *Cell* 1997;90:523–535.
5. Mayer A, Wickner W, Haas A. Sec18p (NSF)-driven release of Sec17p (alpha-SNAP) can precede docking and fusion of yeast vacuoles. *Cell* 1996;85:83–94.
6. Ryu JK, Min D, Rah SH, Kim SJ, Park Y, Kim H, Hyeon C, Kim HM, Jahn R, Yoon TY. Spring-loaded unraveling of a single SNARE complex by NSF in one round of ATP turnover. *Science* 2015;347:1485–1489.
7. Stenbeck G. Soluble NSF-attachment proteins. *Int J Biochem Cell Biol* 1998;30:573–577.
8. Whiteheart SW, Griff IC, Brunner M, Clary DO, Mayer T, Buhrow SA, Rothman JE. SNAP family of NSF attachment proteins includes a brain-specific isoform. *Nature* 1993;362:353–355.
9. Jahn R, Scheller RH. SNAREs—engines for membrane fusion. *Nat Rev Mol Cell Biol* 2006;7:631–643.
10. Zhao M, Wu S, Zhou Q, Vivona S, Cipriano DJ, Cheng Y, Brunger AT. Mechanistic insights into the recycling machine of the SNARE complex. *Nature* 2015;518:61–67.
11. Malhotra V, Orci L, Glick BS, Block MR, Rothman JE. Role of an N-ethylmaleimide-sensitive transport component in promoting fusion of transport vesicles with cisternae of the Golgi stack. *Cell* 1988;54:221–227.
12. Block MR, Glick BS, Wilcox CA, Wieland FT, Rothman JE. Purification of an N-ethylmaleimide-sensitive protein catalyzing vesicular transport. *Proc Natl Acad Sci U S A* 1988;85:7852–7856.
13. Erzberger JP, Berger JM. Evolutionary relationships and structural mechanisms of AAA+ proteins. *Annu Rev Biophys Biomol Struct* 2006;35:93–114.
14. Matveeva EA, He P, Whiteheart SW. N-Ethylmaleimide-sensitive fusion protein contains high and low affinity ATP-binding sites that are functionally distinct. *J Biol Chem* 1997;272:26413–26418.
15. Whiteheart SW, Schraw T, Matveeva EA. N-ethylmaleimide sensitive factor (NSF) structure and function. *Int Rev Cytol* 2001;207:71–112.
16. Yu RC, Hanson PI, Jahn R, Brunger AT. Structure of the ATP-dependent oligomerization domain of N-ethylmaleimide sensitive factor complexed with ATP. *Nat Struct Biol* 1998;5:803–811.
17. May AP, Misura KM, Whiteheart SW, Weis WI. Crystal structure of the amino-terminal domain of N-ethylmaleimide-sensitive fusion protein. *Nat Cell Biol* 1999;1:175–182.

18. Lenzen CU, Steinmann D, Whiteheart SW, Weis WI. Crystal structure of the hexamerization domain of N-ethylmaleimide-sensitive fusion protein. *Cell* 1998;94:525–536.
19. Yu RC, Jahn R, Brunger AT. NSF N-terminal domain crystal structure: models of NSF function. *Mol Cell* 1999;4:97–107.
20. Moeller A, Zhao C, Fried MG, Wilson-Kubalek EM, Carragher B, Whiteheart SW. Nucleotide-dependent conformational changes in the N-Ethylmaleimide Sensitive Factor (NSF) and their potential role in SNARE complex disassembly. *J Struct Biol* 2012;177:335–343.
21. Chang LF, Chen S, Liu CC, Pan X, Jiang J, Bai XC, Xie X, Wang HW, Sui SF. Structural characterization of full-length NSF and 20S particles. *Nat Struct Mol Biol* 2012;19:268–275.
22. Furst J, Sutton RB, Chen J, Brunger AT, Grigorieff N. Electron cryo-microscopy structure of N-ethyl maleimide sensitive factor at 11 Å resolution. *EMBO J* 2003;22:4365–4374.
23. Hohl TM, Parlati F, Wimmer C, Rothman JE, Sollner TH, Engelhardt H. Arrangement of subunits in 20 S particles consisting of NSF, SNAPs, and SNARE complexes. *Mol Cell* 1998;2:539–548.
24. Zhou Q, Huang X, Sun S, Li X, Wang HW, Sui SF. Cryo-EM structure of SNAP-SNARE assembly in 20S particle. *Cell Res* 2015;25:551–560.
25. Karplus M, McCammon JA. Molecular dynamics simulations of biomolecules. *Nat Struct Biol* 2002;9:646–652.
26. Zheng W. All-atom and coarse-grained simulations of the forced unfolding pathways of the SNARE complex. *Proteins* 2014;82:1376–1386.
27. Knecht V, Grubmuller H. Mechanical coupling via the membrane fusion SNARE protein syntaxin 1A: a molecular dynamics study. *Biophys J* 2003;84:1527–1547.
28. Bock LV, Hutchings B, Grubmuller H, Woodbury DJ. Chemomechanical regulation of SNARE proteins studied with molecular dynamics simulations. *Biophys J* 2010;99:1221–1230.
29. Tekpinar M, Zheng W. Unzipping of neuronal snare protein with steered molecular dynamics occurs in three steps. *J Mol Model* 2014;20:2381.
30. Risselada HJ, Grubmuller H. How SNARE molecules mediate membrane fusion: recent insights from molecular simulations. *Curr Opin Struct Biol* 2012;22:187–196.
31. Marrink SJ, Tieleman DP. Molecular dynamics simulation of spontaneous membrane fusion during a cubic-hexagonal phase transition. *Biophys J* 2002;83:2386–2392.
32. Kasson PM, Kelley NW, Singhal N, Vrljic M, Brunger AT, Pande VS. Ensemble molecular dynamics yields submillisecond kinetics and intermediates of membrane fusion. *Proc Natl Acad Sci U S A* 2006;103:11916–11921.
33. Klepeis JL, Lindorff-Larsen K, Dror RO, Shaw DE. Long-timescale molecular dynamics simulations of protein structure and function. *Curr Opin Struct Biol* 2009;19:120–127.
34. Zhao M, Brunger AT. Recent advances in deciphering the structure and molecular mechanism of the aaa+ atpase n-ethylmaleimide-sensitive factor (NSF). *J Mol Biol* 2015, published online 3 November 2015.
35. Tozzini V. Coarse-grained models for proteins. *Curr Opin Struct Biol* 2005;15:144–150.
36. Tozzini V. Minimalist models for proteins: a comparative analysis. *Q Rev Biophys* 2010;43:333–371.
37. Atilgan AR, Durell SR, Jernigan RL, Demirel MC, Keskin O, Bahar I. Anisotropy of fluctuation dynamics of proteins with an elastic network model. *Biophys J* 2001;80:505–515.
38. Tama F, Sanejouand YH. Conformational change of proteins arising from normal mode calculations. *Protein Eng* 2001;14:1–6.
39. Zheng W, Doniach S. A comparative study of motor-protein motions by using a simple elastic-network model. *Proc Natl Acad Sci U S A* 2003;100:13253–13258.
40. Krebs WG, Alexandrov V, Wilson CA, Echols N, Yu H, Gerstein M. Normal mode analysis of macromolecular motions in a database framework: developing mode concentration as a useful classifying statistic. *Proteins* 2002;48:682–695.
41. Zheng W. Coarse-grained modeling of the structural states and transition underlying the powerstroke of dynein motor domain. *J Chem Phys* 2012;136:155103.
42. Zheng W. Normal-mode-based modeling of allosteric couplings that underlie cyclic conformational transition in F(1) ATPase. *Proteins* 2009;76:747–762.
43. Zheng W, Brooks BR, Thirumalai D. Allosteric transitions in the chaperonin GroEL are captured by a dominant normal mode that is most robust to sequence variations. *Biophys J* 2007;93:2289–2299.
44. Bahar I, Rader AJ. Coarse-grained normal mode analysis in structural biology. *Curr Opin Struct Biol* 2005;15:586–592.
45. Tama F, Brooks CL. Symmetry, form, and shape: guiding principles for robustness in macromolecular machines. *Annu Rev Biophys Biomol Struct* 2006;35:115–133.
46. Yang L, Song G, Jernigan RL. Protein elastic network models and the ranges of cooperativity. *Proc Natl Acad Sci U S A* 2009;106:12347–12352.
47. Hinsen K, Petrescu A, Dellerue S. Harmonicity in slow protein dynamics. *Chem Phys* 2000;261:25–37.
48. Zheng W, Auerbach A. Decrypting the sequence of structural events during the gating transition of pentameric ligand-gated ion channels based on an interpolated elastic network model. *PLoS Comput Biol* 2011;7:e1001046.
49. Zorman S, Rebane AA, Ma L, Yang G, Molski MA, Coleman J, Pincet F, Rothman JE, Zhang Y. Common intermediates and kinetics, but different energetics, in the assembly of SNARE proteins. *eLife* 2014;3:e03348.
50. Gao Y, Zorman S, Gundersen G, Xi Z, Ma L, Sirinakis G, Rothman JE, Zhang Y. Single reconstituted neuronal SNARE complexes zipper in three distinct stages. *Science* 2012;337:1340–1343.
51. Zheng W, Brooks BR, Doniach S, Thirumalai D. Network of dynamically important residues in the open/closed transition in polymerases is strongly conserved. *Structure* 2005;13:565–577.
52. Zheng W, Brooks BR, Thirumalai D. Low-frequency normal modes that describe allosteric transitions in biological nanomachines are robust to sequence variations. *Proc Natl Acad Sci U S A* 2006;103:7664–7669.
53. Zheng W, Tekpinar M. Large-scale evaluation of dynamically important residues in proteins predicted by the perturbation analysis of a coarse-grained elastic model. *BMC Struct Biol* 2009;9:45.
54. Zheng W, Qin F. A combined coarse-grained and all-atom simulation of TRPV1 channel gating and heat activation. *J Gen Physiol* 2015;145:443–456.
55. Tekpinar M, Zheng W. Predicting order of conformational changes during protein conformational transitions using an interpolated elastic network model. *Proteins* 2010;78:2469–2481.
56. Zheng W, Brooks B. Identification of dynamical correlations within the myosin motor domain by the normal mode analysis of an elastic network model. *J Mol Biol* 2005;346:745–759.
57. Yang LW, Bahar I. Coupling between catalytic site and collective dynamics: a requirement for mechanochemical activity of enzymes. *Structure* 2005;13:893–904.
58. Zheng W. Toward decrypting the allosteric mechanism of the ryanodine receptor based on coarse-grained structural and dynamic modeling. *Proteins* 2015;83:2307–2318.
59. Zhao C, Matveeva EA, Ren Q, Whiteheart SW. Dissecting the N-ethylmaleimide-sensitive factor: required elements of the N and D1 domains. *J Biol Chem* 2010;285:761–772.
60. Marz KE, Lauer JM, Hanson PI. Defining the SNARE complex binding surface of alpha-SNAP: implications for SNARE complex disassembly. *J Biol Chem* 2003;278:27000–27008.